


# Constructing Janus SnSSe and graphene heterostructures as promising anode materials for Li-ion batteries

Wenxue Zhang<sup>1</sup> | Jiahui Zhang<sup>2</sup> | Cheng He<sup>2</sup>  | Tongtong Li<sup>2</sup>

<sup>1</sup>School of Materials Science and Engineering, Chang'an University, Xi'an, China

<sup>2</sup>State Key Laboratory for Mechanical Behavior of Materials, School of Materials Science and Engineering, Xi'an Jiaotong University, Xi'an, China

## Correspondence

Cheng He, State Key Laboratory for Mechanical Behavior of Materials, School of Materials Science and Engineering, Xi'an Jiaotong University, Xi'an 710049, China.

Email: hecheng@mail.xjtu.edu.cn

## Funding information

National Natural Science Foundation of China, Grant/Award Number: 51471124; Natural Science Foundation of Shaanxi province, China, Grant/Award Numbers: 2020JM-218, 2019JM-189; National Undergraduate Training Program for Innovation and Entrepreneurship, Grant/Award Number: 201810710128; National Key R&D Program of China, Grant/Award Number: 2018YFB0905600

## Summary

Developing efficient anode materials for Li-ion batteries is becoming increasingly important but is still challenging to collect relevant information about their adsorption and diffusion. Herein, by means of density functional theory (DFT) computations, the Janus SnSSe, and graphene van der Waals heterostructures (ie, SSnSe/G and SeSnS/G) are systematically investigated by first principles calculations, aiming at constructing promising anode materials for Li-ion batteries (LIBs). The results have demonstrated that the SnSSe/G heterostructures exhibits a semimetal-to-metal transition after incorporating Li, indicating enhanced conductivity compared to monolayer Janus SnSSe or graphene. Moreover, the SnSSe/G heterostructures can maintain favorable structural stability and ultra-high stiffness well after applying the strain or adsorption of lithium atoms, thereby ensuring the pulverization resistance. In addition, the energy barriers of Li atoms diffusion are very low, which are expected to achieve a fast charge/discharge rate. Meanwhile, the estimated storage capacity of Li on SnSSe/G heterostructures could achieve 472.66 mA h g<sup>-1</sup>, which greatly improves the storage capacity. These interesting results show that Janus SnSSe/G heterostructures could be used as excellent anode materials for LIBs.

## KEYWORDS

anode material, first principles, heterostructure, Janus, Li-ion batteries

## 1 | INTRODUCTION

At present, the booming smart electronics market and growing demand for advanced battery systems have led to a great deal of research work on the high-performance electrode materials.<sup>1-6</sup> As commercial electrochemical cells, Li-ion batteries (LIBs) have a wide range of applications in many fields, like telephones, computers, as well as in current rechargeable cars<sup>7-10</sup> due to the tremendous advantages of dense energy densities,<sup>11,12</sup> large storage capacities,<sup>13-16</sup> long-term cyclabilities,<sup>17-19</sup> and huge electromotive force.<sup>20,21</sup> The single-layered structure of graphene obtained through experiments is used in electrode materials due to its larger specific surface areas,

lower diffusion barrier, and wider voltage window.<sup>22,23</sup> So far, graphene has achieved great success as an anode material for LIBs.<sup>24-26</sup> The adsorption energy of Li is relatively small during the graphite cycling process, resulting in the easy formation of metal clusters and lower storage capacity (370 mA h g<sup>-1</sup>).<sup>27</sup> And other two-dimensional materials such as transition metal dichalcogenides (TMDs),<sup>28,29</sup> black phosphorene (BP),<sup>30,31</sup> and borophene<sup>32,33</sup> with a similar structure to graphene have been widely discussed to characterize the electronic and chemical properties as anode candidates of LIBs. However, most of the monolayer anode materials have many disadvantages, for example, fast capacity decay and weak conductivity for TMDs,<sup>34</sup> rapid capacity loss for

phosphorene,<sup>35</sup> slower charge, and discharge rates for borophene.<sup>33</sup> Hence, there are many strategies to improve the electrochemical performance via these 2D materials with graphene to form heterostructures using as LIBs anodes, including BP/G,<sup>27</sup> MoS<sub>2</sub>/graphene,<sup>36</sup> VS<sub>2</sub>/graphene,<sup>37</sup> MXenes/graphene,<sup>38</sup> and g-C<sub>3</sub>N<sub>4</sub>/graphene.<sup>39</sup> However, satisfactory electrodes with favorable conductivity, outstanding cycle performance, and rate capability remains a challenge.

TMDs with typical layered structure have huge potential in energy storage, because of the weak interlayer van der Waals force and their unique properties.<sup>40,41</sup> Among TMDs, tin dichalcogenides have obtained wide attention due to their excellent electrochemical advantages and abundant reserves.<sup>42,43</sup> For example, SnS<sub>2</sub>, which is a representative of layered hexagonal CdI<sub>2</sub>-type structure, has attracted great interest as the anode of LIBs because of the high theoretical capacities, facile design of size and morphology, and low cost.<sup>44</sup> However, the band gap of the SnS<sub>2</sub> monolayer is 2.1 eV, leading to its relatively poor conductivity.<sup>45,46</sup> The low intrinsic conductivity results in slow dynamics, poor rate characteristics, and rapid capacity decay when used as electrode materials of LIBs at large operating current.<sup>47</sup> Compared with SnS<sub>2</sub>, the band gap of the SnSe<sub>2</sub> monolayer is relatively smaller (1.14 eV), but its conductivity still needs to be further improved.<sup>48</sup> Then, we propose to construct Janus monolayer SnSSe to adjust the size of the band gap and electrical properties simultaneously. Moreover, groundbreaking studies have shown that doping a part of sulfur element in selenide could increase the concentration of electron and hole carriers, thereby improving the conductivity. Simultaneously, the sulfuration on selenides can enhance the donor states of the surface sulfur.<sup>49,50</sup> The SnSSe monolayer electrodes produced by simple ball-mill mixing and scraper-coating technology have shown good cycle stability and rate capability at distinct discharge cut-off voltages,<sup>51</sup> which are different from the traditional layered TMD material with mirror-symmetrical structure. The Janus SnSSe monolayer is asymmetric, and the Sn atoms in the middle layer are bonded to the S and Se atoms on each side by covalent bonds. In particular, SnSSe monolayer has an intrinsic dipole perpendicular to the plane and the internal electric field generated thereby, which can greatly improve carrier mobility. Although SnSSe monolayer is a viable option as the anode material, the electrical conductivity and mechanical strength cannot really meet the needs of LIBs, so these properties need to be further improved. Depending on the outstanding electrical conductivity of graphene, it is interesting to verify whether SnSSe and graphene heterostructures can be served as ideal anode materials for high-performance LIBs.

In this paper, the geometric structures, electrochemical performance, and diffusion properties of Li atoms on the SnSSe/graphene van der Waals heterostructures (SnSSe/G) have been evaluated by the first-principles calculation. The SnSSe/G heterostructures as materials for LIBs have higher stiffness and electrical conductivity, and lower energy Li diffusion barrier. Moreover, the SnSSe/G heterostructures could hold up to five Li atomic layers and still ensure negative adsorption energy, thereby significantly increasing lithium intercalation capacity. The study offers crucial opinions into SnSSe/G heterostructures and investigates their application potential in effective commercial electrode materials for LIBs with higher storage capacities and good conductivity.

## 2 | CALCULATION METHODS

In this work, the Vienna Ab initio Simulation Package (VASP) with the projector-augmented-wave (PAW) was used to carry out all density functional theory (DFT) calculations.<sup>52-54</sup> In order to treat the electron-electron exchange correlation, the Perdew-Burke-Ernzerhof (PBE) form of the generalized gradient approximation (GGA) was used.<sup>55</sup> In order to correct the effect of nontrivial Van der Waals force, the DFT-D2 method proposed by Grimme was selected.<sup>56-59</sup> All the atomic positions were fully relaxed until the forces were less than 0.01 eV Å<sup>-1</sup> and the energy difference was below 10<sup>-5</sup> eV. For plane-wave expansion of the electron eigenfunction, a cutoff energy of 500 eV was selected. The *k*-point mesh of the Brillouin area for structural optimization calculations is set to 7 × 7 × 1. A vacuum spacing of 25 Å was added along the direction perpendicular to the 2D nanosheets to avoid the interaction between neighboring layers. For calculating the adsorption and diffusion characteristics of lithium, a 2 × 2 × 1 SnSSe/G supercell was selected to guarantee that there are sufficient areas for Li migration. In order to estimate the energy barrier for Li atoms migration, the climbing image nudged elastic band (CI-NEB) method was employed.<sup>60</sup> CI-NEB was a small improvement of NEB, which can effectively determine the transition states and the minimum energy paths (MEPs) for generalized solid-state transformations and fixed cell.<sup>61,62</sup> For the calculation part of mechanical properties, Poisson's ratio  $\nu_2$  and elastic modulus  $Y_s$  were expressed as below:

$$\varepsilon_x = \nu_1 - \nu_2 \varepsilon_y \quad (1)$$

$$Y_s = \left( \frac{1}{A_0} \right) * \left( \frac{\partial^2 E(k)}{\partial k^2} \right). \quad (2)$$

### 3 | RESULTS AND DISCUSSION

Considering vdW interaction, SnSSe/G heterostructures were obtained by stacking SnSSe and graphene monolayers in the vertical direction.<sup>63,64</sup> The structural parameters of the original Janus SnSSe and graphene monolayers are firstly checked before constructing SnSSe/G heterostructures. The calculated lattice constants of SnSSe and graphene supercells after geometric optimization are 3.68 and 2.47 Å, separately, which are in good agreement with the reported values. In order to construct the SnSSe/G heterostructures with 0.86% mismatch, the  $2 \times 2$  supercell of the SnSSe is used to match the  $3 \times 3$  supercell of graphene. Moreover, the atoms on each side of SnSSe monolayer are S and Se atoms, so two stacked configurations are within our consideration and marked as SSnSe/G and SeSnS/G heterostructures in Figure 1A,C, respectively. To quantitatively check the thermodynamic stability of SnSSe/G heterostructures, the binding energy ( $E_b$ ) is defined as:

$$E_b = E_{\text{SnSSe/G}} - E_{\text{SnSSe}} - E_G, \quad (3)$$

where  $E_{\text{SnSSe/G}}$ ,  $E_{\text{SnSSe}}$ , and  $E_G$  represent the total energies of SnSSe/G, isolated SnSSe, and graphene monolayer, separately. The estimated values of  $E_b$  are negative ( $E_b = -0.684$  and  $-0.780$  eV for SSnSe/G and SeSnS/G heterostructures), which indicate that the synthesis of SSnSe/G and SeSnS/G are feasible. The atomic and band structures of the SnSSe monolayer were calculated and presented in Figure S1 Data S1.<sup>65</sup> It can be seen that SnSSe monolayer is an indirect semiconductor with the band gap ( $E_g$ ) of 1.372 eV. After contacting, the band gaps of the two proposed SnSSe/G heterostructures become 0 (Figure 1B,D), which can extremely improve the electronic conductivity by the subjoin of a single-layer graphene to the SnSSe layer. The band structure indicates that SnSSe/G heterostructures provide great advantages compared with the semiconducting SnSSe monolayer, and thus satisfying the requirements of high conductivity.

To check the adsorption capacity of Li atoms, the adsorption properties of Li on SSnSe/G and SeSnS/G heterostructures are further studied. The distinct adsorption sites of one Li atom on the SSnSe/G and SeSnS/G heterostructures are shown in Figure 2A,B. There are two typical adsorption sites: (a) Li adsorption on the outside surface of SnSSe (Li/SSnSe/G and LiSeSnS/G), and (b) Li adsorption in the interlayer of the SSnSe/G and SeSnS/G (SSnSe/Li/G and SeSnS/Li/G). For Li/SSnSe/G (Li/SeSnS/G), there are two Li-adsorption sites on the SnSSe surface: Li adsorbed on the center of a hexagon ring composed by Sn and S atoms ( $H_{\text{Se}}$ -site for Li/SSnSe/G and  $H_{\text{S}}$ -site for LiSeSnS/G) and Li on top Sn

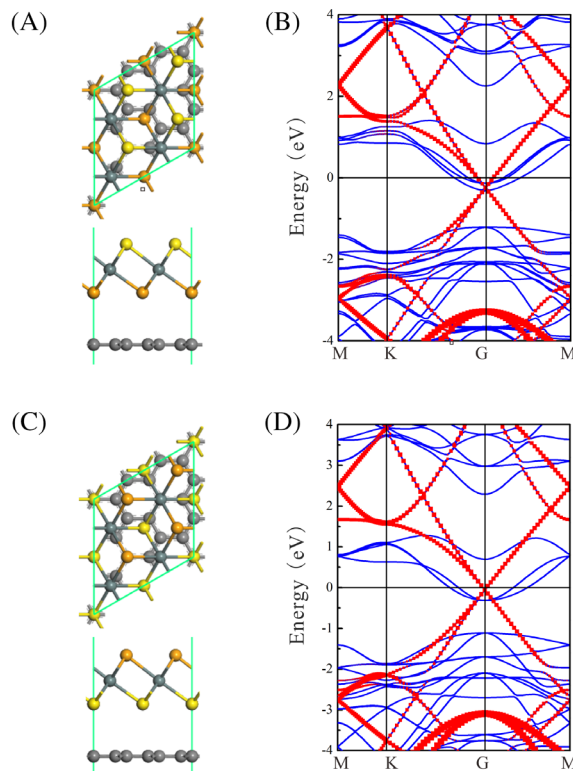


**FIGURE 1** A, Optimized structure and B, band structure of SSnSe/G; C, Optimized structure and D, band structure of SeSnS/G. The gray ball represents the C atom, the yellow ball represents the S atom, the orange ball represents the Se atom, and the dark blue ball represents the Sn atom [Colour figure can be viewed at [wileyonlinelibrary.com](http://wileyonlinelibrary.com)]

atom ( $T_1$ -site for Li/SSnSe/G and  $T_2$ -site for LiSeSnS/G); For SSnSe/Li/G (SeSnS/Li/G), there are two adsorption sites:  $H_1$ -site and  $H_2$ -site for SSnSe/Li/G ( $H_3$ -site and  $H_4$ -site for SeSnS/Li/G). After geometrically optimizing the Li-adsorption positions of SnSSe/G heterostructures, no significant structural deformation is discovered. The adsorption energy ( $E_{\text{ads}}$ ) for these Li-adsorption positions of the SnSSe/G heterostructures is defined as:

$$E_{\text{ads}} = E_{\text{SnSSe/G + Li}} - E_{\text{SnSSe/G}} - nE_{\text{Li}}/n, \quad (4)$$

where  $E_{\text{SnSSe/G + Li}}$ ,  $E_{\text{SnSSe/G}}$ , and  $E_{\text{Li}}$  represent the energy of the lithiated SnSSe/G, SnSSe/G, and an isolated Li atom, separately.  $n$  represents the amount of Li adatoms. According to the definition of  $E_{\text{ads}}$ , a more negative value means a more stable structure of the Li atoms combined with SnSSe/G, and vice versa. The comparative  $E_{\text{ads}}$  of the Li-adsorption positions are shown in Table 1.  $E_{\text{ads}}$  for  $H_{\text{Se}}$ -site and  $H_{\text{S}}$ -site adsorption sites are more negative when Li adatom is adsorbed on SnSSe. The Li adatom embedded in the vdW interface of SnSSe/G prefers to be at  $H_1$ -site ( $E_{\text{ads}} = -4.148$  eV) for the SSnSe/G and  $H_3$ -site ( $E_{\text{ads}} = -4.067$  eV) for the SeSnS/G, which are more

stable than that on the SnSse surface since Li in the interface interacts with both graphene and SnSse layers of SnSse/G. Thus, the construction of the SnSse/G heterostructures can extremely increase the binding energy of Li atoms and SnSse (graphene), which can avoid the appearance of Li metal clusters, thereby improving the reversibility and safety of LIBs.

It is well-known that the mechanical properties of anode materials may change significantly during the lithiation process. Moreover, the structural damage caused by Li-adsorption can change its morphology or lead to the electrode fracture, resulting in large capacity attenuation and poor cycle capacity. Thus, we focus on the in-plane mechanical stability of SnSse/G heterostructures. Poisson's ratio is the ratio of transverse strain to axial strain, and it provides a normal way to compare the structural properties of real materials. In Equation (1),

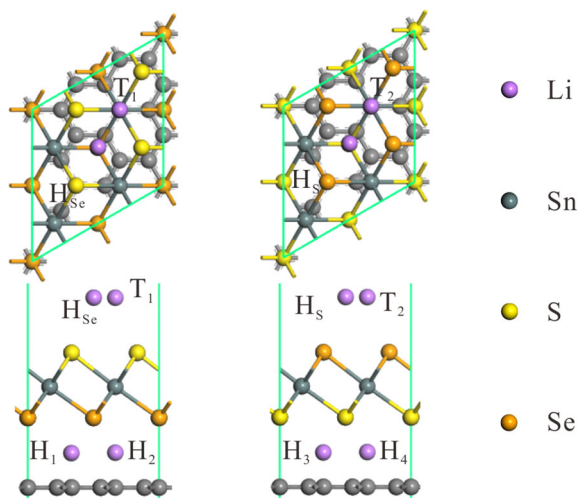


**FIGURE 2** Top and side views of the lattice structure and Li-adsorption sites in A, SSnSe/G and B, SeSnS/G [Colour figure can be viewed at [wileyonlinelibrary.com](http://wileyonlinelibrary.com)]

the linear Poisson's ratio describing the structural performance is the first-order coefficient ( $\nu_2$ ). Since SnSse/G heterostructures are anisotropic materials obviously,  $\nu_2$  in both  $a$  and  $b$  orientation are obtained. After applying strain on SSnSe/G and SeSnS/G along  $a$  or  $b$  orientation, the strain generated simultaneously in another orientation is shown in Figure S2 in Data S1 and the linear Poisson's ratio  $\nu_2$  are in Table 2. The value of  $\nu_2$  for the SSnSe/G along the  $a$  orientation ( $\nu_2 = 0.088$ ) is slightly larger than that along  $b$  orientation ( $\nu_2 = 0.083$ ), reflecting the larger rigidity along  $b$  orientation than that along  $a$  orientation. Conversely, this value along the  $b$  orientation ( $\nu_2 = 0.117$ ) is larger than that along  $a$  direction ( $\nu_2 = 0.099$ ) for the SeSnS/G, which means the rigidity along  $a$  orientation is larger than along  $b$  orientation. Next, DFT calculations are used to obtain the elastic modulus defined by Griffith. Figure 3 shows the schematic of the SSnSe/G and SeSnS/G heterostructures under uniaxial strain along the  $a$  and  $b$  orientation. When uniaxial strain is applied to the SSnSe/G heterostructure in  $a$  and  $b$  orientation and the elastic modulus is 385.48 and 368.32 N/m, as seen in Figure 3A,B. Similarly, Figure 3C,D are applying strain to the SeSnS/G heterostructure and the elastic modulus is 359.21 and 363.28 N/m, respectively. The elastic modulus of the SSnSe/G heterostructure in both directions are larger than that of the SeSnS/G system, indicating that the SSnSe/G heterostructure has higher hardness, strength, and ductility. The ultrahigh elastic modulus of SnSse/G heterostructure is desirable for LIBs anodes, which can avoid the structural damage caused by lithium insertion.

Since the power factor of electronic equipment is largely determined by the current conversion efficiency, the deformation potential approximation (DPA) method with an effective mass approximation is used to calculate the carrier mobility ( $u$ ):

System	Site	$E_{\text{ads}}$ (eV)	$D_{\text{Li-S}}$ (Å)	$D_{\text{Li-Se}}$ (Å)	$D_{\text{Li-C}}$ (Å)	$\Delta Q$ (e)
SSnSe/G	$H_{\text{Se}}$	-3.755	2.413	-	-	0.588
	$T_1$	-3.726	2.425	-	-	0.623
	$H_1$	-4.148	-	2.594	2.407	0.520
	$H_2$	-4.012	-	2.615	2.403	0.649
SeSnS/G	$H_{\text{S}}$	-3.431	-	2.458	-	0.581
	$T_2$	-3.420	-	2.503	-	0.620
	$H_3$	-4.067	2.466	-	2.196	0.603
	$H_4$	-4.046	2.503	-	2.195	0.719

**TABLE 1** Calculated structural and electronic properties for Li atoms adsorbed on supercell of the SSnSe/G and SeSnS/G systems

Note:  $E_{\text{ads}}$  represented the adsorption energy;  $D_{\text{Li-S}}$ ,  $D_{\text{Li-Se}}$ , and  $D_{\text{Li-C}}$  refer to minimal distances of Li-S, Li-Se, and Li-C.  $\Delta Q$  is the charge transfer of Li atoms.



$$\mu = \frac{e\hbar^3 Y_S}{k_B T m^* E_1^2}, \quad (5)$$

$$m^* = \hbar^2 \left[ \frac{\partial E(k)}{\partial k^2} \right]^{-1}, \quad (6)$$

where  $e$ ,  $\hbar(=h/2\pi)$ ,  $k_B$ ,  $Y_S$ , and  $T$  stand for the charge of electron, Planck's constant, Boltzmann constant, elastic constant, and temperature (300 K in the current situation), respectively.  $E_1$  represents the deformation potential constant and the expression is  $E_1 = \Delta V/(\Delta l/l_0)$ .  $\Delta V$  stands for the energy change when the cell is appropriately expanded or contracted.  $l_0$  and  $\Delta l$  represent the lattice parameter along the transmission direction and the deformation of lattice parameter, separately. Effective mass ( $m^*$ ) is calculated by the following formula:

**TABLE 2** Poisson's ratio  $\nu_2$ , elastic constant  $Y_S$  (N/m), deformation potential  $E_1$  (eV), effective mass  $m^*$  ( $m_0$ ), carrier mobility  $\mu$  ( $10^4 \text{ cm}^2 \text{ V}^{-1} \text{ s}^{-1}$ ) for the SSnSe/G, and SeSnS/G, respectively

		$\nu_2$	$Y_S$	$E_1$	$m$	$\mu$
SSnSe/G	$h_x$	0.088	385.48	3.448	0.371	0.499
	$e_x$			3.407	-0.117	5.146
	$h_y$	0.083	368.32	3.325	0.371	0.513
	$e_y$			3.078	-0.117	6.025
SeSnS/G	$h_x$	0.099	359.21	3.941	0.301	0.542
	$e_x$			2.750	-0.113	7.891
	$h_y$	0.117	363.28	2.709	0.301	1.159
	$e_y$			4.762	-0.113	2.661

where  $E$  and  $k$  represent wave vector the energy.  $m^*$  and  $E_1$  can be calculated from the band structures. The various calculation results of Poisson's ratio, elastic constant, deformation potential, effective mass, and carrier mobility along  $a$  and  $b$  orientation of SnSSe/G heterostructures are given in Table 2. It can be found that  $m^*$  of electron and hole of the SSnSe/G heterostructure is  $-0.117 m_0$  and  $0.371 m_0$ , which is larger than that of the SeSnS/G heterostructure ( $m_e = -0.113$  and  $m_h = 0.301$ ). The calculations prove that the SeSnS/G system has higher hole mobility than SSnSe/G system, while it also has higher electron mobility than SSnSe/G system along  $a$  orientation. Hence, on the whole, the SeSnS/G system has better electron/hole mobility performance than SSnSe/G system. Meanwhile, it is also worth to note that the hole/electron mobility along the  $b$  orientation is higher than the  $a$  orientation, which is probably because of the difference in Janus SnSSe/G arrangement.

To discuss the electronic conductivity of the SnSSe/G heterostructures upon Li atom intercalation, the electron density of state (DOS), and partial density of state (PDOS) of SnSSe/G, Li/SnSSe/G, and SnSSe/Li/G systems are investigated in Figure 4. In Figure 4A, the maximum peak of DOS near Fermi energy ( $E_f$ ) is between  $-2.480$  and  $-0.713$  eV for SSnSe/G, between  $-3.048$  and  $-1.861$  eV for SSnSe/Li/G, and between  $-3.201$  and  $-2.283$  eV for Li/SSnSe/G. In Figure 4B, the maximum

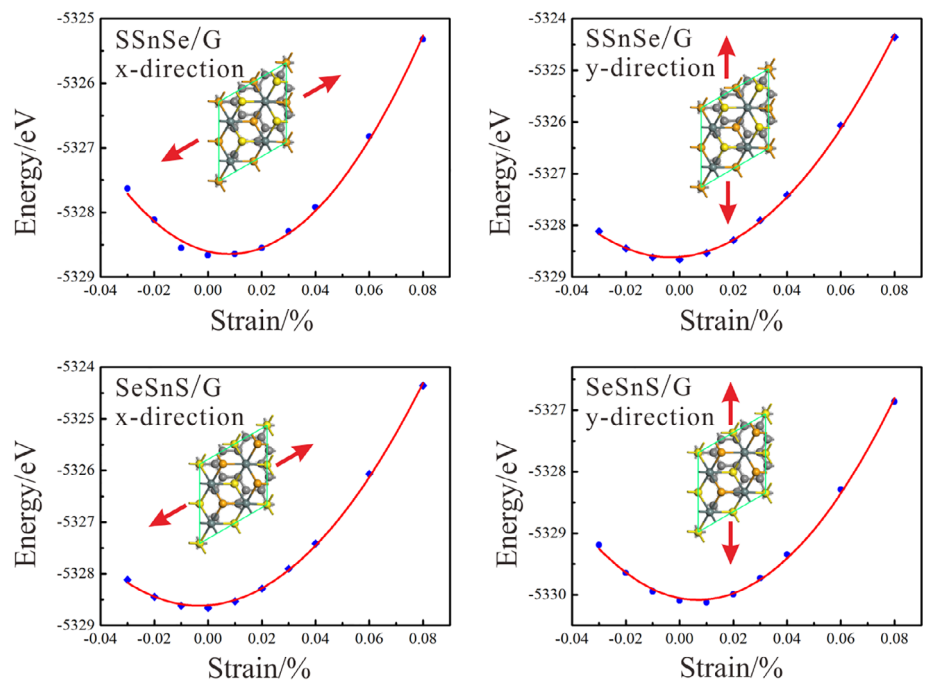


**FIGURE 3** Alteration of strain energy with the applied A, a direction strain and B, b direction strain for SSnSe/G; C, a direction strain and D, b direction strain for SeSnS/G [Colour figure can be viewed at [wileyonlinelibrary.com](http://wileyonlinelibrary.com)]

peak of DOS near  $E_f$  is between  $-2.421$  and  $-1.040$  eV for the SeSnS/G, between  $-3.013$  and  $-1.804$  eV for SeSnS/Li/G and between  $-3.131$  and  $-1.910$  eV for Li/SeSnS/G. The position of the largest peak has shifted slightly to the left and the number of conduction bands of the heterostructure has increased after Li-adsorption, which mean that a partial charge transfer occurred and the stability of the system has been slightly improved. From PDOS of Li/SnSSe/G and SnSSe/Li/G systems (Figure 4C-F), the largest peak is mostly contributed by the S and Se atoms. Besides, the orbitals near  $E_f$  is mostly contributed by the Sn, S, and Se atoms, indicating hybridization between those orbitals and a covalent bond character. For the case of Li adsorption on SnSSe surface (Li/SSnSe/G and Li/SeSnS/G), the orbitals of Li and SnSSe overlap, which is a characteristic of hybridization. For another case of Li incorporation into SnSSe/G (SSnSe/Li/G and SeSnS/Li/G), the orbitals of Li and SnSSe or graphene overlap, which indicates that there is a covalent hybrid interaction between the adsorbed Li and SnSSe or graphene layer. Thus, the types of bonds between Li and the SnSSe/G heterostructures are mainly ionic bonds, and some covalent bond components in part. Besides, both of SSnSe/G and SeSnS/G systems become metallic characteristics without band gaps after lithiation treatment. Therefore, the electronic conductivity can be improved by building the heterostructure of graphene and SnSSe monolayers, thereby meeting the requirements of the anode material for high electronic conductivity.

To visualize the mechanism of Li-insertion at different sites of the SnSSe/G substrate, the charge density difference is calculated with the following equation:

$$\Delta\rho(z) = \rho(z)_{\text{SnSSe/G} + \text{Li}} - \rho(z)_{\text{SnSSe/G}} - \rho(z)_{\text{Li}}, \quad (7)$$

where  $\rho(z)_{\text{SnSSe/G} + \text{Li}}$ ,  $\rho(z)_{\text{SnSSe/G}}$ , and  $\rho(z)_{\text{Li}}$  represent the charge density of Li incorporation into SnSSe/G, SnSSe/G, and isolated Li atoms, separately. The charge density difference of Li atoms incorporation into SnSSe monolayer and SnSSe/G systems are shown in Figure 5. In all cases, the gain of electrons and the loss of electrons are shown by blue and red, separately. For the case of Li-adsorption on the SnSSe monolayer (Figure 5A), the gain and the net loss of electronic charge appear directly on SnSSe monolayer and above the Li atoms. Since the electronegativity of Li is smaller than that of Se (S), the electrons are transferred from Li to adjacent Se or S, which leads to the formation of a strong ionic bond. When Li atom is adsorbed on SnSSe surface (Figure 5B), charge transfer is similar to the SnSSe monolayer. However, since the distance between Li and the graphene layer is relatively long, no electron is accumulated in the graphene layer. For the situation of Li atom incorporation into the interlayer of the SnSSe/G (Figure 5C), since the electronegativity of Li is also smaller than that of C, electrons are simultaneously transferred from Li atom to SnSSe and graphene layer, which indicates that a strong ionic-bond is formed between the two layers and the embedded Li atom.

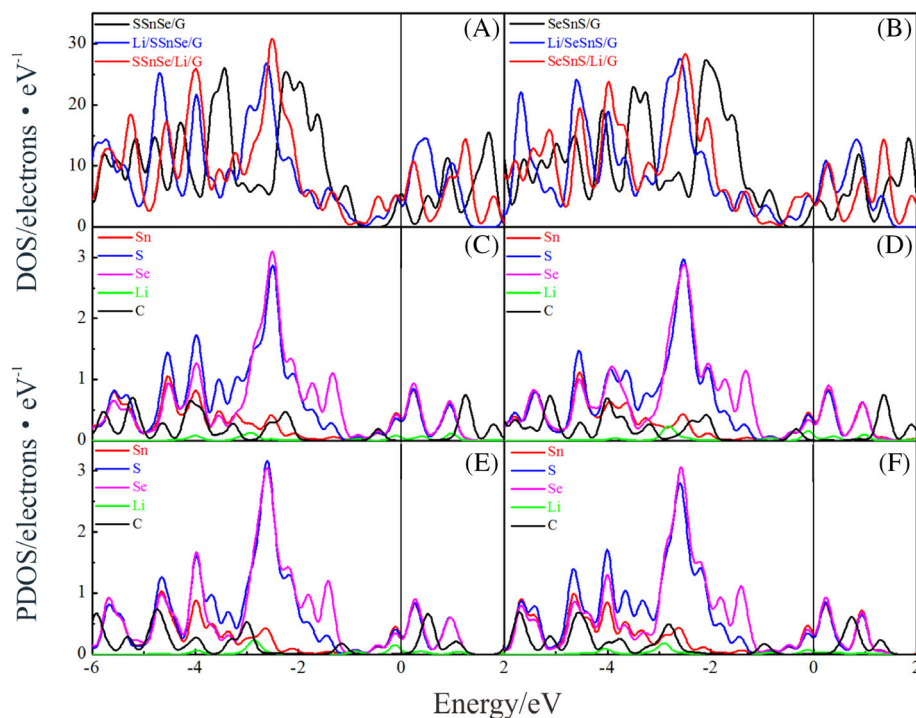


**FIGURE 4** A,B, DOS of SnSSe/G and Li adsorbed on SnSSe/G, from C-F, PDOS Li adsorbed on SSnSe/G and SeSnS/G. The Fermi level is set to zero [Colour figure can be viewed at [wileyonlinelibrary.com](http://wileyonlinelibrary.com)]

The migration performance of LIBs mainly determines the fast charge and discharge capability, therefore the energy barrier for Li diffusion on the SnSSe/G heterostructures is further analyzed. The diffusion behavior of Li atoms on the surface of SnSSe and the intermediate layer of SnSSe/G heterostructures is calculated respectively. The possible diffusion paths and the energy barrier of Li diffusion on monolayer SnSSe and the SnSSe outer surface of SnSSe/G are firstly discussed by NEB calculations. When Li on S side of SnSSe surface, the optimized migration pathway for the Li atom is from an energetic  $H_{Se}$ -site to a neighboring  $H_{Se}$ -site via the  $T_1$ -site (Figure 6B), labels  $H_{Se}-T_1-H_{Se}$ . The corresponding energy barrier is 0.25 eV, which is slightly larger than SnSSe monolayer (0.24 eV), as seen in Figure 6A. When Li on Se side of the SnSSe surface seen in Figure 6C, Li migrates from  $H_S$ -site through  $T_2$ -site to a neighboring  $H_S$ -site ( $H_S-T_2-H_S$ ), the corresponding energy barrier is 0.26 eV, which is also a bit larger than that of SnSSe monolayer (0.25 eV), as seen in Figure 6D. The comparative larger energy barrier of Li migration on the SnSSe outer surface is mostly due to the influence of graphene layer. Although the graphene layer is far away from Li atom, it also has a certain effect on the Li atom, resulting in a larger resistance of Li diffusion on SnSSe surface.

Next, the diffusion paths and energy barriers of Li incorporation into the interlayer of SnSSe/G heterostructures have been discussed. Since influenced by the combined interaction of Li atom and the other two layers, the diffusion paths and energy barriers are different from that of SnSSe monolayer. The migration route of Li is along the trajectory of a series of purple spheres shown in Figure 7, where  $H_1$ -site ( $H_3$ -site) is taken as the starting position since it is the most stable position. The diffusion paths for SSnSe/Li/G and SeSnS/Li/G are along the direction of  $H_1-T_1'-H_1'-T_2'-H_1$  and  $H_3-T_3'-H_3'-T_4'-H_3$ , respectively. Our calculated migration energy barriers for SSnSe/Li/G and SeSnS/Li/G are 0.35 and 0.33 eV, respectively, which is slightly larger compared to that on SnSSe

surface. However, the energy barriers of Li diffusion are still lower than that of some other TMDs heterostructure materials (0.47 eV for  $MoS_2/Ti_2CF_2$  and 0.57 eV for  $MoS_2/Ti_2CO_2$ ).<sup>66-68</sup> The calculation results of the migration barrier indicate that the diffusion processes on SnSSe/G heterostructures are energetically favorable, indicating that SnSSe/G heterostructures can be used as reliable LIBs electrodes.

After studying diffusion paths and energy barriers, the theoretical capacity of high-content lithium is calculated finally. In order to find out the largest capacity of Li adatoms, the trend of the average  $E_{ads}$  of Li atoms with its concentration ( $x$ ) at three sides of the SnSSe/G heterostructures have been calculated: SnSSe surface, graphene surface, and interlayer, as shown in Figure 8.  $E_{ads}$  of interlayer ( $-3.473$  eV for SSnSe/G and  $-2.678$  eV for SeSnS/G) are more negative than that of SnSSe surface and graphene surface when only one Li atoms layer is adsorbed on the SnSSe/G heterostructures ( $x = 0.5$ ), indicating that Li atoms prefer to adsorb in the interlayer. Since  $E_{ads}$  of SnSSe surface is more negative than that of graphene surface, two Li atoms layers preferentially adsorb in the interlayer and SnSSe surface. Hence, the optimal configurations of Li-ions adsorption on the SnSSe/G heterostructures for different Li concentrations are shown in Figure 8C,D, and the corresponding chemical formula is  $Li_xSnSSe/G$ . Especially, when all the stable adsorption positions are filled with Li atoms (12 Li atoms,  $x = 1.5$ ),  $E_{ads}$  are  $-2.538$  and  $-2.273$  eV, separately. These relatively negative values of  $E_{ads}$  can ensure the favorable stability and safety of lithium on the SnSSe/G heterostructures.  $E_{ads}$  decreases with the increasing of Li contents due to the enhancement of Li-Li repulsion at relatively higher Li concentration. With the continuous increase of the Li concentration,  $E_{ads}$  gradually decreases, which is mainly because of the enhancement of Li-Li repulsive force. To further increase lithium storage levels, another Li atomic layer (20 Li atoms) is added, which covers the outside surface of SnSSe and graphene, separately. Although the two outermost Li atomic layers are

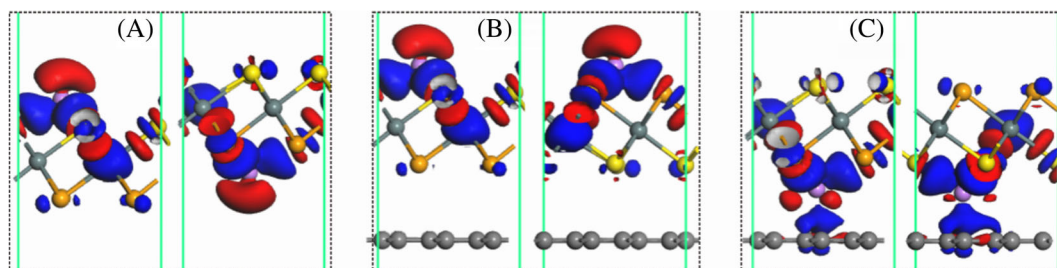


**FIGURE 5** Differential charge densities of Li adsorbed A, on the SnSSe surface, B, on the SnSSe surface of the SnSSe/G and C, in the interlayer of the SnSSe/G. Blue and red colors indicate the electron accumulation and depletion, respectively [Colour figure can be viewed at [wileyonlinelibrary.com](http://wileyonlinelibrary.com)]

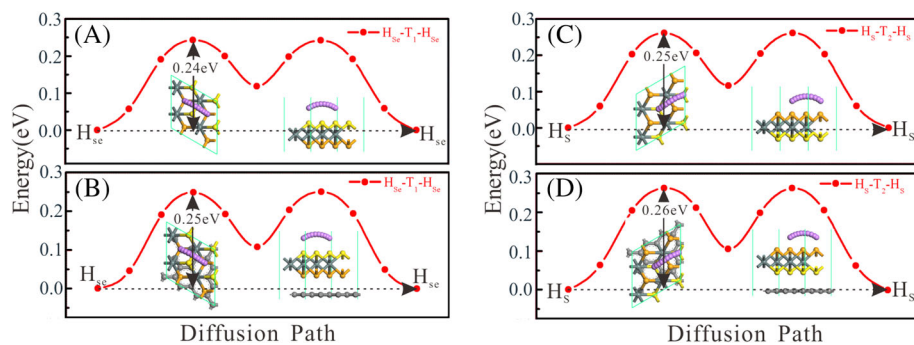


**FIGURE 6** Diffusion energy barrier of one Li atom diffusion on A, SSnSe, B, SnSSe surface of SSnSe/G, C, SeSnS, and D, SnSSe surface of SeSnS/G [Colour figure can be viewed at wileyonlinelibrary.com]

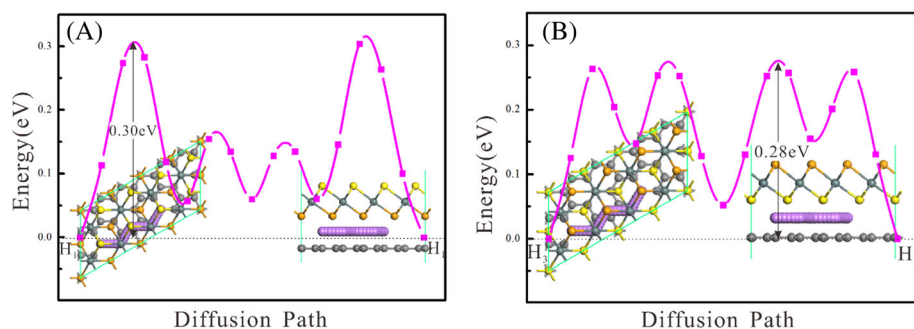


**FIGURE 7** Diffusion pathways and energy barrier of one Li atom diffusion in the interlayer of A, SSnSe/G and B, SeSnS/G [Colour figure can be viewed at wileyonlinelibrary.com]

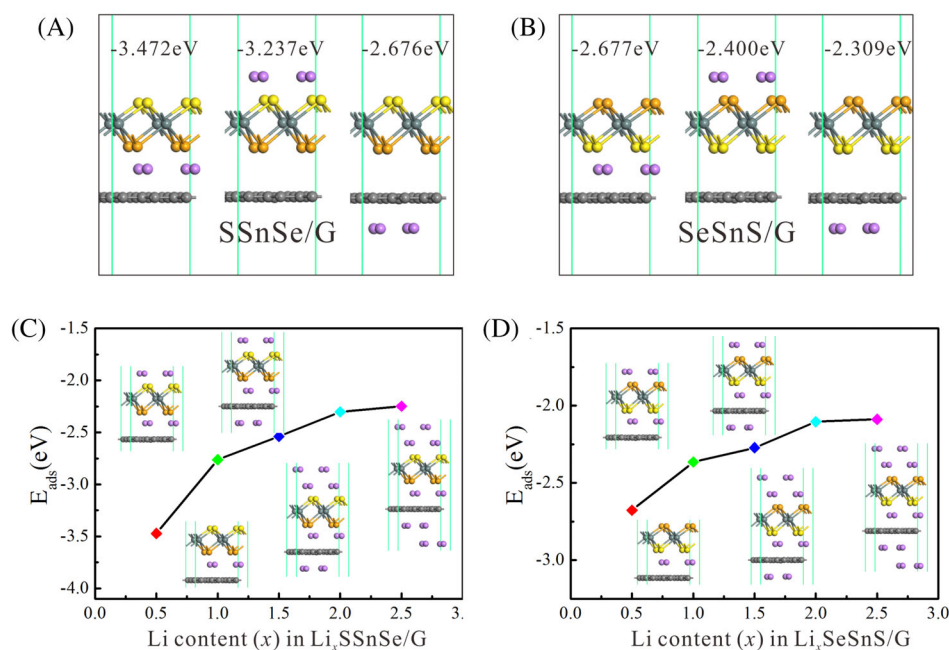


**FIGURE 8** One Li atoms layer adsorbed on interlayer, SnSSe surface and graphene surface of A, SSnSe/G and B, SeSnS/G heterostructure. Adsorption energy of Li atoms as a function of  $x$  in C,  $\text{Li}_x\text{SSnSe/G}$  and D,  $\text{Li}_x\text{SeSnS/G}$  [Colour figure can be viewed at wileyonlinelibrary.com]

slightly far away from the SnSSe/G heterostructure,  $E_{\text{ads}}$  obtained are still negative, and  $E_{\text{ads}}$  of SSnSe/G is  $-2.248$  eV (the value of SSnSe/G is  $-2.089$  eV), indicating the system energy is stable. It can be inferred that the SnSSe/G heterostructures can hold up to five Li atomic layers and significantly increase lithium intercalation capacity. The largest storage capacity ( $C_M$ ) can be calculated by:  $C_M = \frac{xF}{M_{\text{SnSSe/G}}}$ , where  $x$ ,  $F$ , and  $M_{\text{SnSSe/G}}$  stand for

the composition of Li in  $\text{Li}_x\text{SnSSe/G}$ , Faraday constant ( $26.8 \text{ Ah mol}^{-1}$ ), and mass of SnSSe/G, separately. The estimated storage capacity of Li on the SnSSe/G heterostructures is  $472.66 \text{ mAh g}^{-1}$ , which is higher than some other heterostructure anode materials, such as MoSSe/G ( $390.00 \text{ mAh g}^{-1}$ ),<sup>69</sup> BP/TiC<sub>2</sub> ( $430.33 \text{ mAh g}^{-1}$ ),<sup>70</sup> and GeSe/BP ( $191.8 \text{ mAh g}^{-1}$ ).<sup>71</sup> Meanwhile, according to our calculated results,  $C_m$  of SnSSe/G heterostructures is



also higher than SnS<sub>2</sub> (293.15 mAh g<sup>-1</sup>), SnSe (406.73 mAh g<sup>-1</sup>) and graphene (374 mAh g<sup>-1</sup>). Hence, the results of calculation indicate the SnSSe/G heterostructures have broad application prospects in high-capacity LIBs electrode materials.

## 4 | CONCLUSION

In summary, the adsorption and diffusion of Li on SnSSe/G heterostructures have been explored in a systematic way. The results demonstrated that the electronic conductivity of SnSSe/G heterostructures is significantly higher than that of SnSSe monolayer, and SnSSe/G heterostructures possess ultrahigh stiffness and maintain the high diffusion mobility of Li. Furthermore, the lower energy barriers are found for Li atoms on SnSSe surface and in the interlayer of SnSSe/G heterostructures, which are expected to achieve a fast charge/discharge rate. Finally, the estimated storage capacity of Li on SnSSe/G heterostructures could achieve 472.66 mA h g<sup>-1</sup>. These results indicate that the SnSSe/G heterostructures can be applied as suitable anode materials in LIBs, and also provide guidance for experimentally preparing high-performance SnSSe/G heterostructures as LIBs.

## ACKNOWLEDGEMENTS

The authors acknowledge supports by National Natural Science Foundation of China (NSFC, No. 51471124), Natural Science Foundation of Shaanxi province, China (2020JM-218, 2019JM-189), National Key R&D Program of China (2018YFB0905600), National Undergraduate Training Program for Innovation and Entrepreneurship (201810710128).

## DATA AVAILABILITY STATEMENT

The data that support the findings of this study are available from the corresponding author upon reasonable request.

## ORCID

Cheng He  <https://orcid.org/0000-0002-6612-5346>

## REFERENCES

- Zhao CY, Wang X, Kong JH, et al. Self-assembly-induced alternately stacked single-layer MoS<sub>2</sub> and N-doped graphene: a novel van der Waals heterostructure for lithium-ion batteries. *ACS Appl Mater Interfaces*. 2016;8(3):2372-2379.
- Shi J, Wang Z, Fu YQ. A critical review on progress of the electrode materials of vanadium redox flow battery. *Int J Energy Res*. 2020;44:7903-7923.
- Arvas MB, Gencten M, Sahin Y. A two-dimensional material for high capacity supercapacitors: S-doped graphene. *Int J Energy Res*. 2019;44:1624-1635.
- Wang Z, Niu X, Xiao J, Wang C, Liu J, Gao F. First principles prediction of nitrogen-doped carbon nanotubes as a high-performance cathode for Li-S batteries. *RSC Adv*. 2013;3(37):16775-16780.
- Fu Q, Cao H, Liang G, et al. A highly Li<sup>+</sup>-conductive HfNb<sub>24</sub>O<sub>62</sub> anode material for superior Li<sup>+</sup> storage. *Chem Commun*. 2020;56(4):619-622.
- Zhu X, Liang G, Fu Q, et al. An inverse opal Cu<sub>2</sub>Nb<sub>34</sub>O<sub>87</sub> anode for high-performance Li<sup>+</sup> storage. *Chem Commun*. 2020;56(53):7321-7324.
- Crabtree G. The energy-storage revolution. *Nature*. 2015;526(7575):S92-S92.
- Fairley P. Energy storage: power revolution. *Nature*. 2015;526(7575):S102-S104.
- Ramadesigan V, Northrop PWC, De S, Santhanagopalan S, Braatz RD, Subramanian VR. Modeling and simulation of lithium-ion batteries from a systems engineering perspective. *J Electrochem Soc*. 2012;159(3):R31-R45.
- Hou CX, Wang B, Murugadoss V, et al. Recent advances in Co<sub>3</sub>O<sub>4</sub> as anode materials for high-performance lithium-ion batteries. *Eng Sci*. 2020;11:19-30.
- Tarascon JM, Armand M. Issues and challenges facing rechargeable lithium batteries. *Nature*. 2001;414(6861):359-367.
- Li D, Dai PC, Chen Y, Peng RW, Sun Y, Zhou HS. Lithium borocarbide LiBC as an anode material for rechargeable Li-ion batteries. *J Phys Chem C*. 2018;122(32):18231-18236.
- Li QF, Yang JC, Zhang L. Theoretical prediction of blue phosphorene/borophene heterostructure as a promising anode material for lithium-ion batteries. *J Phys Chem C*. 2018;122(32):18294-18303.
- Luo LL, Zhao P, Yang H, et al. Surface coating constraint induced self-discharging of silicon nanoparticles as anodes for lithium ion batteries. *Nano Lett*. 2015;15(10):7016-7022.
- Fu YX, Pei XYN, Dai Y, Mo DC, Lyu S. Three-dimensional graphene-like carbon prepared from CO<sub>2</sub> as anode material for high-performance lithium-ion batteries. *ES Energy Environ*. 2019;4:66-73.
- Liu M, Yang Z, Sun H, et al. A hybrid carbon aerogel with both aligned and interconnected pores as interlayer for high-performance lithium-sulfur batteries. *Nano Res*. 2016;9:3735-3746.
- Ji LW, Lin Z, Alcoutlabi M, Zhang XW. Recent developments in nanostructured anode materials for rechargeable lithium-ion batteries. *Energy Environ Sci*. 2011;4(8):2682-2699.
- Li RJ, Lin CF, Wang N, et al. Advanced composites of complex Ti-based oxides as anode materials for lithium-ion batteries. *Adv Compos Hybrid Mater*. 2018;1(3):440-459.
- Yang ZY, Zhang P, Wang J, et al. Hierarchical carbon@SnS<sub>2</sub> aerogel with "skeleton/skin" architectures as a high-capacity, high-rate capability and long cycle life anode for sodium ion storage. *ACS Appl Mater Interfaces*. 2018;10:37434-37444.
- Reddy MV, Rao GVS, Chowdari BVR. Metal oxides and oxysalts as anode materials for Li ion batteries. *Chem Rev*. 2013;113(7):5364-5457.
- Jing Y, Zhou Z, Cabrera CR, Chen ZF. Graphene, inorganic graphene analogs and their composites for lithium ion batteries. *J Mater Chem A*. 2014;2(31):12104-12122.
- Novoselov KS, Geim AK, Morozov SV, et al. Electric field effect in atomically thin carbon films. *Science*. 2004;306(5696):666-669.
- Britnell L, Gorbachev RV, Jalil R, et al. Field-effect tunneling transistor based on vertical graphene heterostructures. *Science*. 2012;335(6071):947-950.

24. Yoo E, Kim J, Hosono E, Zhou H-S, Kudo T, Honma I. Large reversible Li storage of graphene nanosheet families for use in rechargeable lithium ion batteries. *Nano Lett.* 2008;8(8):2277-2282.
25. Park M-S, Yu J-S, Kim KJ, et al. One-step synthesis of a sulfur-impregnated graphene cathode for lithium-sulfur batteries. *Phys Chem Chem Phys.* 2012;14(19):6796-6804.
26. Wang H, Yang Y, Liang Y, et al. Graphene-wrapped sulfur particles as a rechargeable lithium-sulfur battery cathode material with high capacity and cycling stability. *Nano Lett.* 2011;11(7):2644-2647.
27. Guo GC, Wang D, Wei XL, et al. First-principles study of phosphorene and graphene heterostructure as anode materials for rechargeable Li batteries. *J Phys Chem Lett.* 2015;6(24):5002-5008.
28. Yang E, Ji H, Jung Y. Two-dimensional transition metal dichalcogenide mono layers as promising sodium ion battery anodes. *J Phys Chem C.* 2015;119(47):26374-26380.
29. Jing Y, Zhou Z, Cabrera CR, Chen Z. Metallic VS<sub>2</sub> monolayer: a promising 2D anode material for lithium ion batteries. *J Phys Chem C.* 2013;117(48):25409-25413.
30. Sun J, Lee H-W, Pasta M, et al. A phosphorene-graphene hybrid material as a high-capacity anode for sodium-ion batteries. *Nat Nanotechnol.* 2015;10(11):980-U184.
31. Kulish VV, Malyi OI, Persson C, Wu P. Phosphorene as an anode material for Na-ion batteries: a first-principles study. *Phys Chem Chem Phys.* 2015;17(21):13921-13928.
32. Liu J, Zhang L, Xu L. Theoretical prediction of borophene monolayer as anode materials for high-performance lithium-ion batteries. *Ionics.* 2018;24(6):1603-1615.
33. Zhang X, Hu J, Cheng Y, Yang HY, Yao Y, Yang SA. Borophene as an extremely high capacity electrode material for Li-ion and Na-ion batteries. *Nanoscale.* 2016;8(33):15340-15347.
34. Xiang P, Chen X, Liu J, Xiao B, Yang L. Borophene as conductive additive to boost the performance of MoS<sub>2</sub>-based anode materials. *J Phys Chem C.* 2018;122(17):9302-9311.
35. Ren X, Lian P, Xie D, et al. Properties, preparation and application of black phosphorus/phosphorene for energy storage: a review. *J Mater Sci.* 2017;52(17):10364-10386.
36. Sljivancanin Z, Belic M. Graphene/MoS<sub>2</sub> heterostructures as templates for growing two-dimensional metals: predictions from ab initio calculations. *Phys Rev Mater.* 2017;1(4):044003.
37. Mikhaleva NS, Visotin MA, Kuzubov AA, Popov ZI. VS<sub>2</sub>/graphene heterostructures as promising anode material for Li-ion batteries. *J Phys Chem C.* 2017;121(43):24179-24184.
38. Cakir D, Sevik C, Gulseren O, Peeters FM. Mo<sub>2</sub>C as a high capacity anode material: a first-principles study. *J Mater Chem A.* 2016;4(16):6029-6035.
39. Senthil C, Kesavan T, Bhaumik A, Sasidharan M. N-rich graphitic carbon nitride functionalized graphene oxide nanosheet hybrid as anode for high performance lithium-ion batteries. *Mater Res Express.* 2018;5(1):016307
40. Yu J, Xu C-Y, Li Y, et al. Ternary SnS<sub>2-x</sub>Sex alloys nanosheets and nanosheet assemblies with tunable chemical compositions and band gaps for photodetector applications. *Sci Rep.* 2015;5:17109
41. Liu Y, Kang H, Jiao L, et al. Exfoliated-SnS<sub>2</sub> restacked on graphene as a high-capacity, high-rate, and long-cycle life anode for sodium ion batteries. *Nanoscale.* 2015;7(4):1325-1332.
42. Zhang Z, Zhao X, Li J. SnSe/carbon nanocomposite synthesized by high energy ball milling as an anode material for sodium-ion and lithium-ion batteries. *Electrochim Acta.* 2015;176:1296-1301.
43. Li Z, Ding J, Mitlin D. Tin and tin compounds for sodium ion battery anodes: phase transformations and performance. *Acc Chem Res.* 2015;48(6):1657-1665.
44. Seo J-W, Jang J-T, Park S-W, Kim C, Park B, Cheon J. Two-dimensional SnS<sub>2</sub> nanoplates with extraordinary high discharge capacity for lithium ion batteries. *Adv Mater.* 2008;20(22):4269-4273.
45. Huang Y, Chen X, Zhou D, et al. Stabilities, electronic and optical properties of SnSe<sub>2(1-x)</sub>S<sub>2x</sub> alloys: a first-principles study. *J Phys Chem C.* 2016;120(10):5839-5847.
46. Lee PA, Said G, Davis R, Lim TH. On optical properties of some layer compounds. *J Phys Chem Solids.* 1969;30(12):2719.
47. Zhang Y, Yang J, Zhang Y, et al. Fe<sub>2</sub>O<sub>3</sub>/SnS<sub>2</sub> hexagonal nanoplates as lithium-ion batteries anode. *ACS Appl Mater Interfaces.* 2018;10(15):12722-12730.
48. Choi J, Jin J, Jung IG, Kim JM, Kim HJ, Son SU. SnSe<sub>2</sub> nanoplate-graphene composites as anode materials for lithium ion batteries. *Chem Commun.* 2011;47(18):5241-5243.
49. Xie W, Populoh S, Galazka K, et al. Thermoelectric study of crossroads material MnTe via sulfur doping. *J Appl Phys.* 2014;115(10):103707
50. Mehta RJ, Karthik C, Jiang W, et al. High electrical conductivity antimony selenide nanocrystals and assemblies. *Nano Lett.* 2010;10(11):4417-4422.
51. Wang XS, Chen D, Yang ZH, et al. Novel metal chalcogenide SnS<sub>2</sub> as a high-capacity anode for sodium-ion batteries. *Adv Mater.* 2016;28(39):8645-8650.
52. Kresse G, Furthmuller J. Efficient iterative schemes for ab initio total-energy calculations using a plane-wave basis set. *Phys Rev B.* 1996;54(16):11169-11186.
53. Sham LJ, Kohn W. One-particle properties of an inhomogeneous interacting electron gas. *Phys Rev.* 1966;145(2):561.
54. Blochl PE. Projector augmented-wave method. *Phys Rev B.* 1994;50(24):17953-17979.
55. Perdew JP, Burke K, Ernzerhof M. Generalized gradient approximation made simple. *Phys Rev Lett.* 1996;77(18):3865-3868.
56. Grimme S. Semiempirical GGA-type density functional constructed with a long-range dispersion correction. *J Comput Chem.* 2006;27(15):1787-1799.
57. Stöhr M, Van Voorhis T, Tkatchenko A. Theory and practice of modeling van der Waals interactions in electronic-structure calculations. *Chem Soc Rev.* 2019;48(15):4118-4154.
58. Su G, Yang S, Li S, et al. Switchable Schottky contacts: simultaneously enhanced output current and reduced leakage current. *J Am Chem Soc.* 2019;141(4):1628-1635.
59. Su G, Yang S, Jiang Y, et al. Modeling chemical reactions on surfaces: the roles of chemical bonding and van der Waals interactions. *Prog Surf Sci.* 2019;94(4):100561.
60. Henkelman G, Jonsson H. Improved tangent estimate in the nudged elastic band method for finding minimum energy paths and saddle points. *J Chem Phys.* 2000;113(22):9978-9985.
61. Zarkevich NA, Johnson DD. Nudged-elastic band method with two climbing images: finding transition states in complex energy landscapes. *J Chem Phys.* 2015;142(2):5.
62. Sheppard D, Xiao PH, Chemelewski W, Johnson DD, Henkelman G. A generalized solid-state nudged elastic band method. *J Chem Phys.* 2012;136(7):8.

63. Dong MM, He C, Zhang WX. Tunable electronic properties of arsenene and transition-metal dichalcogenide heterostructures: a first-principles calculation. *J Phys Chem C*. 2017;121:22040-22048.
64. He C, Zhang JH, Zhang WX, Li TT. Type-II InSe/G-C<sub>3</sub>N<sub>4</sub> heterostructure as a high-efficiency oxygen evolution reaction catalyst for photoelectrochemical water splitting. *J Phys Chem Lett*. 2019;10:3122-3128.
65. Li TT, He C, Zhang WX. A novel porous C<sub>4</sub>N<sub>4</sub> monolayer as a potential anchoring material for lithium-sulfur battery design. *J Mater Chem A*. 2019;7:4134-4144.
66. Li J, Peng Q, Zhou J, Sun Z. MoS<sub>2</sub>/Ti<sub>2</sub>CT<sub>2</sub> (T= F, O) heterostructures as promising flexible anodes for lithium/sodium ion batteries. *J Phys Chem C*. 2019;123(18):11493-11499.
67. Zhang M, Tang C, Cheng W, Fu L. The first-principles study on the performance of the graphene/WS<sub>2</sub> heterostructure as an anode material of Li-ion battery. *J Alloys Compd*. 2021;855:157432.
68. Shi L, Zhao TS, Xu A, Xu JB. Ab initio prediction of a silicene and graphene heterostructure as an anode material for Li- and Na-ion batteries. *J Mater Chem A*. 2016;4(42):16377-16382.
69. Zhou SH, Zhang J, Ren ZZ, et al. First-principles study of MoS<sub>2</sub>/graphene heterostructures as anode for Li-ion batteries. *Chem Phys*. 2020;529:110583.
70. Peng Q, Hu K, Sa B, et al. Unexpected elastic isotropy in a black phosphorene/TiC<sub>2</sub> van der Waals heterostructure with flexible Li-ion battery anode applications. *Nano Res*. 2017;10:3136-3150.
71. He C, Zhang JH, Zhang WX, Li TT. GeSe/BP van der Waals heterostructures as promising anode materials for potassium-ion batteries. *J Phys Chem C*. 2019;123:5157-5163.

## SUPPORTING INFORMATION

Additional supporting information may be found online in the Supporting Information section at the end of this article.

**How to cite this article:** Zhang W, Zhang J, He C, Li T. Constructing Janus SnSSe and graphene heterostructures as promising anode materials for Li-ion batteries. *Int J Energy Res*. 2021;1-11. <https://doi.org/10.1002/er.6519>